ORIGINAL RESEARCH

D.J. Cross
J.A. Flexman
Y. Anzai
T. Sasaki
P.M. Treuting
K.R. Maravilla
S. Minoshima

In Vivo Manganese–MR Imaging of Calcium Influx in Spontaneous Rat Pituitary Adenoma

BACKGROUND AND PURPOSE: Rapid uptake of the calcium analog manganese (Mn^{2+}) into spontaneous pituitary adenoma during MR imaging of aged rats generated the hypothesis that neuroendocrine tumors may have a corresponding increase in calcium influx required to trigger hormonal release. A goal of this study was to investigate the potential for clinical evaluation of pituitary adenoma by MR imaging combined with administration of Mn^{2+} (Mn-MR imaging).

MATERIALS AND METHODS: Mn-MR imaging was used to characterize the dynamic calcium influx in normal aged rat pituitary gland as well as spontaneous pituitary adenoma. To confirm the validity of Mn^{2+} as a calcium analog, we inhibited Mn^{2+} uptake into the olfactory bulb and pituitary gland of normal rats by using the calcium channel blocker verapamil. Rats with adenomas received fluorodeoxyglucose–positron-emission tomography (FDG-PET) scanning for characterization of tumor metabolism. Mn^{2+} influx was characterized in cultured pituitary adenoma cells.

RESULTS: Volume of interest analysis of the normal aged pituitary gland versus adenoma indicated faster and increased calcium influx in adenoma at 1, 3, 11, and 48 hours. Mn^{2+} uptake into the olfactory bulb and pituitary gland of normal rats was inhibited by calcium channel blockers and showed dose-dependent inhibition on dynamic MR imaging. FDG-PET indicated correlation between tumor energy metabolism and Mn^{2+} influx as well as tumor size.

CONCLUSION: These results indicate that adenomas have increased activity-dependent calcium influx compared with normal aged pituitary glands, suggesting a potential for exploitation in the clinical work-up of pituitary and other neuroendocrine tumors by developing Mn-MR imaging for humans.

In recent years, studies from several groups have used manganese (Mn^{2+}), a paramagnetic calcium analog, combined with MR imaging to study aspects of brain anatomy and neuronal function.[1-5] In one study, Mn^{2+} combined with serial MR imaging (Mn-MR imaging) and statistical brain mapping were used to investigate normal trans-synaptic axonal transport through the rat olfactory system.[6]

Mn^{2+} ions enter cells via voltage-gated calcium channels,[7-9] and this influx has been shown to be activity-dependent.[10,11] This property of Mn^{2+} is well-established and encourages the development of Mn^{2+}-enhanced MR imaging as a calcium influx indicator in various tissues.[12] Neuroendocrine cells, similar to neuronal cells, express calcium channels on the cell membrane. Calcium influx is essential for triggering hormone release in response to action potential membrane depolarization.[13,14] Pituitary adenomas may manifest clinically by hormonal hypersecretion, which is dependent on increased activity-dependent calcium influx.[15,16]

Current clinical work-up for diagnosis and treatment of different types of pituitary adenomas usually includes MR imaging with or without gadolinium contrast enhancement. MR imaging provides morphologic information by using both T1-weighted and fast spin-echo T2-weighted pulse sequences to delineate adenoma from normal tissue.[17] In comparison with more well-established extracellular MR imaging contrast agents such as gadolinium, Mn^{2+} is an intracellular agent. Processes such as cellular uptake, storage, transport, protein binding, and clearance can all be targeted for assessment of pathology and response to treatment.[12]

During the course of an imaging study of aged Sprague Dawley rats, it was discovered that 4 subjects had spontaneous pituitary adenomas. These neuroendocrine tumors were found at the time of serial MR imaging by using manganese chloride ($MnCl_2$) administered intranasally. The discovery of rapid uptake of Mn^{2+} into the adenomas led us to hypothesize that pituitary adenoma would show increased calcium influx, which could be used as an index of tumor activity. This study was designed to investigate further the link between calcium influx and pituitary pathology by using Mn-MR imaging.

We hypothesized that pituitary tumors would have a corresponding increase in the calcium influx required to trigger hormonal release. A goal of this study was to investigate increased calcium influx in pituitary adenomas through the use of MR imaging combined with the administration of Mn^{2+}. In addition, we suggest the potential development of Mn^{2+} as a contrast agent for in vivo functional MR imaging of pituitary and other types of neuroendocrine tumors.

Materials and Methods

Our study consisted of 3 primary components. First, we performed in vivo MR imaging with $MnCl_2$ to characterize the dynamic calcium influx in the normal aged rat pituitary gland as well as spontaneous pituitary adenomas in aged rats. Second, to confirm the validity of Mn^{2+} as a calcium analog, we inhibited Mn^{2+} uptake into the olfactory bulb and pituitary gland of normal young rats by using the calcium channel blocker verapamil and assessed Mn^{2+} uptake by using

Received January 8, 2007; accepted after revision April 3.

From the Washington National Regional Primate Center (D.J.C., S.M.) and the Departments of Radiology (Y.A., T.S., K.R.M., S.M.), Bioengineering (J.A.F., S.M.), and Comparative Medicine (P.M.T.), University of Washington, Seattle, Wash; and the Neuroscience Program (D.J.C., S.M.), University of Michigan, Ann Arbor, Mich.

This study was supported in part by a Washington Alzheimer Disease Research Center Pilot grant and Washington National Primate Research Center grant NCRR P51 RR000166.

A portion of this paper was previously presented at: Annual Meeting of the Society for Neuroscience, November 12–16, 2005; Washington, DC.

Please address correspondence to Satoshi Minoshima, MD, PhD, Department of Radiology, University of Washington, 1959 NE Pacific St, BB201c, Box 357115, Seattle, WA 98195-7115; e-mail: minoshim@u.washington.edu

DOI 10.3174/ajnr.A0693

dynamic MR imaging. Aged rats with adenomas received additional scanning by using fluorodeoxyglucose–positron-emission tomography (FDG-PET) for further characterization of tumor glucose metabolism. Last, we performed in vitro characterization of Mn^{2+} influx into cultured GH3 pituitary adenoma cells. Details of these experiments are in the following paragraphs.

Subjects

A total of 16 rats (14 male, 2–22 months of age; Sprague Dawley, Charles River Laboratories, Wilmington, Mass) were used for the in vivo imaging experiments. Originally obtained as part of an aging study, 4 rats (2 male, 18–22 months of age, "aged breeders") had spontaneous pituitary tumors that were discovered at the time of initial MR imaging. Four aged rats (15–18 months) with normal pituitary glands were scanned as a comparison. In addition, 8 young rats were scanned in a calcium channel modulation and blocking experiment. All subjects were kept on a normal 12-hour light/dark cycle and had free access to food and water. All procedures were approved by the University of Washington Animal Care Committee.

Injections and MR imaging

Under isoflurane gas anesthesia, rats received a baseline MR imaging before administration of $MnCl_2$. After the prescanning, in the part of the study involving Mn^{2+} uptake modulation via the calcium channel blocker, young healthy rats (2 months of age, $n = 8$) received one of the following procedures: 1) high-dose verapamil: (3 μL, 5 mg/2 mL) injection into the right nasal cavity, followed after 20 minutes by 8- to 10-μL injection of 1-mol/L $MnCl_2$; 2) medium-dose verapamil: (3 μL, 5 mg/8 mL) injection into right nasal cavity followed after 1 hour by 8- to 10-μL injection of $MnCl_2$; or 3) low-dose verapamil: (3-μL, 5 mg/8 mL) injection into right nasal cavity followed after 4 hours by 8- to 10-μL injection of $MnCl_2$. For MR imaging of normal aged pituitary glands as well as pituitary adenomas, rats ($n = 8$) received only an 8- to 10-μL injection of $MnCl_2$ into the right nasal cavity.[6] Intranasally administered $MnCl_2$ was rapidly absorbed through nasal mucosa into plasma and also taken up by primary olfactory neurons. Serial MR imaging was performed at 1, 3, 11, 24, 48, 72, and 240 hours postinjection in all subjects. During imaging, body temperature was maintained by using an MR imaging–compatible heating pad (Deltaphase Isothermal Pad; Braintree Scientific, Braintree, Mass). Rats were allowed to move freely in their cages between scanning sessions.

T1-weighted images using a 3D spoiled gradient-recalled echo (3D-SPGR) pulse sequence were acquired on a standard 1.5T MR scanner (Signa; GE Healthcare, Milwaukee Wis) with a custom rat brain volume coil. The original acquisition matrix of 256 × 160 and 44 sections was reconstructed to a 256 × 256 image matrix. A 0.5-mm section thickness in 88 continuous sections was obtained by using zero-filled interpolation with the following scanning parameters: FOV = 7 × 4 cm; TE = 6.8 ms; TR = 15 ms; flip angle = 45°; NEX = 4. Total scanning time was 7 minutes 54 seconds. Voxel size for the image dataset before image processing was 0.273 × 0.273 × 0.5 mm.

FDG-PET Scanning of Pituitary Adenoma

In addition to MR imaging, 3 of the rats with spontaneous pituitary tumors underwent PET scanning by using FDG for characterization of tumor energy metabolism and for differentiation of active tumor from necrosis. Under isoflurane gas anesthesia, 0.5-mCi FDG was administered via tail vein injection, followed by a 40-minute uptake period. PET scanning was performed by using a high-resolution scanner (SHR-7700; Hamamatsu Photonics, Hamamatsu, Japan). 2D imaging for 45 minutes acquired 93 interleaved sections with 1.2-mm section thickness, and images were reconstructed by using a filtered back-image projection for an approximate in-plane resolution of 3-mm full width at half maximum.

Image Processing

Both PET and MR imaging sets for a single subject were coregistered to the baseline scan (no Mn^{2+}) by using rigid-body transformation. The algorithm uses mutual information[18] as a cost function and Powell iterative search algorithm to optimize 6 parameters (x y z translation and rotation).[19]

Coregistered image sets from the same subject were transformed to the *Rat Brain in Stereotaxic Coordinates*[20] to allow group-wise, pixel-by-pixel statistical analysis. The coregistered image sets for each subject were matched to an MR stereotactic template corresponding to the atlas.[6] Resultant MR images had an 80 × 80 image matrix of 140 sections with a uniform voxel size of 0.2 mm.

Pixel intensities of MR image sets were normalized to minimize drift in MR sensitivity and differences in intensity across scans and subjects. To remove influence of local Mn^{2+} intensity in normalization, we performed a fine adjustment between individual scans and the template image set from the same subject by using a stochastic normalization algorithm.[21,22] In addition, PET scans were normalized to the global intensity.

In vitro Assessment of Mn^{2+} Uptake into Cultured Cells

Mn^{2+} uptake was evaluated in prolactin- and growth hormone–secreting rat pituitary tumor GH3 cells (ATCC, Manassas, Va). GH3 cells were cultured in Ham F12K medium (ATCC) supplemented with 15% heat-inactivated horse serum and 2.5% heat-inactivated fetal bovine serum with 20-U/mL penicillin-streptomycin in a 5% CO_2 airhumidified atmosphere at 37°C. Approximately 500,000 cells/well in 1 mL of growth medium were seeded in a 12-well plate and stimulated with 2 nM of growth hormone–releasing factor (GHRF; Sigma Aldrich, St Louis, Mo). Two minutes after the addition of GHRF, $MnCl_2$ (Sigma Aldrich) was added in a final concentration of 0, 0.25, or 0.5 mM. Cells were incubated for 4 minutes at room temperature, then removed, washed 3 times, and suspended in phosphate-buffered saline. Samples were acid-digested and Mn^{2+} content was assessed by using inductively coupled plasma mass spectrometry to quantify the amount of Mn^{2+} in each cell. All liquid in samples was initially evaporated, and cells were digested in an acid solution of 3:1 perchloric to nitric acid for 3 hours at 60°C. A calibration curve was first established for various known concentrations of Mn^{2+} to convert the relative values obtained for cell samples to Mn^{2+} content per cell.

Tumor Characterization

Following the final scanning, aged rats with spontaneous pituitary adenomas were euthanized by anesthetic overdose, and brains with adenoma were removed. Adenomas were preserved in 4% paraformaldehyde until histopathologic characterization was performed on individual tumors. Only 3 of the tumors (rats 1–3) were available for pathology due to the unexpected death of 1 subject during a holiday weekend. Tumor samples were processed routinely with paraffin embedding, sectioned at 4–5 μm, followed by hematoxylin-eosin staining (H&E). Tumors were examined histologically by a board-certified veterinary pathologist. To provide further in vivo characterization and corresponding diagnostic information, a board-certified neuroradiologist inspected the MR images of rat brains.

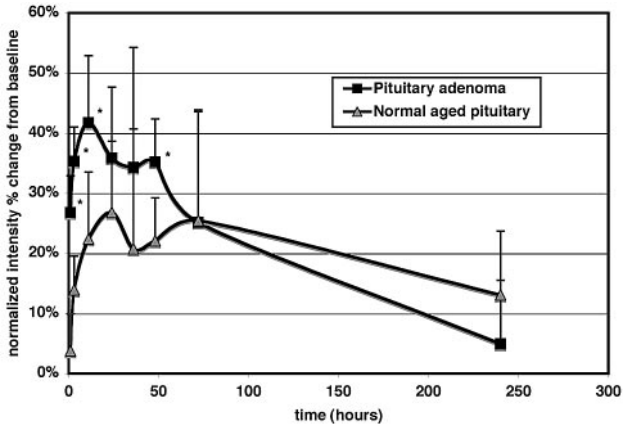

Fig 1. Calcium influx is faster and increased in adenoma versus normal pituitary gland. The vertical axis represents the mean percentage change in intensity from baseline values calculated as the following: (intensity at time point − intensity at baseline) / (intensity at baseline) × 100. The horizontal axis is time in hours postinjection. Error bars show the SD of mean percentage change. The asterisk indicates that differences between the 2 groups reached statistical significance at 1, 3, 11, and 48 hours ($P \leq .05$).

Data Analysis

Standardized volumes of interest (VOIs) (spherical r = 0.5 mm) were placed on coregistered, standardized, and normalized images for all time points in the pituitary gland (or pituitary adenoma) for all subjects as well as in the olfactory bulb of the subjects in the calcium channel blocker study. In addition, VOIs at prescanning and 1 hour postinjection scanning were measured in the carotid artery close to the area of tumor to confirm rapid absorption of intranasally administered $MnCl_2$ into plasma. Changes in MR imaging intensity for these VOIs were calculated by subtracting baseline (preinjection) intensity from postadministration time points. Significant changes in intensity were determined by *t* test ($P \leq .05$). The correlation coefficient was calculated between peak average change in MR imaging intensity, peak FDG uptake on PET scans, and overall tumor volume (as assessed on MR imaging) for the 3 subjects that underwent PET scanning.

Results

Pituitary Adenoma Has a Higher Calcium Influx Than a Normally Aged Pituitary Gland

Dynamic assessment of Mn^{2+} uptake in the normal aged rat pituitary gland versus adenoma indicated that the peak uptake is both faster and greater in adenoma (42 ± 18% at 11 hours and 27 ± 12% at 24 hours for adenoma and normal pituitary gland, respectively) (Fig 1). Changes in uptake, representing altered calcium influx between the 2 groups, were significant at 1, 3, 11, and 48 hours ($P \leq .05$). The dynamic curves indicated that clearance may be altered in adenomas; however, there was no significant difference between subjects after 48 hours. Individual tumors can be easily distinguished on MR images when compared with a normal pituitary gland, even as soon as 1 hour postadministration of $MnCl_2$ (Fig 2). For example, the extent of the tumor in rat 1 can be difficult to distinguish from normal brain tissue before $MnCl_2$ administration but can be clearly seen at 1 hour. Sequential images demonstrate heterogeneous contrast enhancement in pituitary adenomas. VOI analysis of the nearby carotid artery indicated a significant change in signal intensity at 1 hour compared with prescanning (44.5 ± 8.8%, $P \leq .01$), indicating rapid absorption of intranasally administered $MnCl_2$ into plasma. The degree of contrast enhancement (Mn^{2+} uptake) was variable but higher at 11 hours after contrast injection than at 1 hour after injection, indicating slow tumor uptake of the tracer. This gradual uptake is not well explained by the absorption of intranasal Mn^{2+} into plasma but indicates intracellular uptake through calcium channels.

Calcium Channel Blocker Inhibits Mn^{2+} Uptake

We investigated the uptake of Mn^{2+} into normal neuronal cells as well as normal pituitary cells via calcium channels. Using a calcium channel blocker, verapamil, administered at 3 different dose/time intervals, we were able to inhibit the uptake into the olfactory primary neurons in the olfactory bulb (from the olfactory epithelium, site of administration via the olfactory nerve) (Fig 3*A*). Mn^{2+} uptake into the bulb was significantly higher with low-dose verapamil than with medium and high doses at all time points postadministration ($P \leq .05$). However, only at the peak uptake at 24 hours of the medium-dose verapamil was there a significant increase over the high dose. We then looked at the Mn^{2+} uptake in the pituitary gland of these normal rats. Rats receiving a high dose of verapamil intranasally showed the same inhibition of uptake that we saw in the olfactory bulb, which was significant at all time points from medium- and low-dose verapamil (Fig 3*B*). However, pituitary uptake between medium and low doses was nearly identical.

Calcium Influx Is Related to Energy Metabolism and Tumor Size

We performed FDG-PET scanning on 3 of the 4 rats with spontaneous adenomas (1 subject died before the PET scanning). When the average percentage change in MR imaging intensity, reflecting tumor calcium influx, was compared with peak tumor uptake of FDG on PET images as well as with the size of the tumor, there was a general correlation with all of these indices (Table). Calcium influx was most closely correlated to tumor size (Pearson correlation coefficient = 0.99) and also well correlated to peak FDG uptake (Pearson correlation coefficient = 0.91). Peak FDG uptake was less well correlated to tumor size (Pearson correlation coefficient = 0.84). An example of coregistered PET- and Mn^{2+}-enhanced MR images shows good agreement between areas for enhancement and FDG uptake, suggesting that calcium influx may be related to energy metabolism and thus the functional activity of pituitary adenomas (Fig 4).

Mn^{2+} Uptake May Suggest Differences in Tumor Composition

Tumors from subjects 1–3 were removed and stained for pathologic characterization. With some specific differences in individual cellular composition and degree of hemorrhage or numbers of cystic spaces, all of the tumors were classified as pituitary adenomas, typical of "chromophobe adenoma of the pars distalis."[23] Although there were foci of moderate atypia including karyomegaly and anisokaryocytosis in this study, malignancy of the tumors was not determined because invasion to adjacent tissues or intraorgan metastasis could not be assessed fully by histologic analysis.

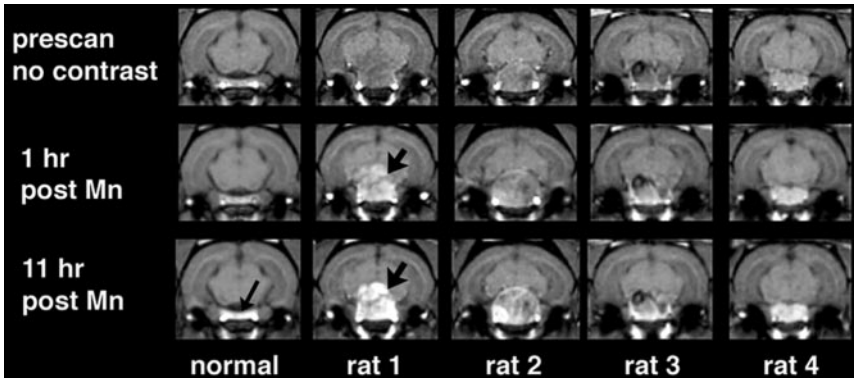

Fig 2. Individual Mn-MR images show enhancement of tumor after 1 hour. First column shows coronal sections of a single representative MR image of normal pituitary enhancement at baseline and 1 and 11 hours postinjection (*small black arrow*). Other columns show coronal sections of each individual subject with pituitary adenoma. Adenomas of individual subjects show clear enhancement at 1 hour postinjection (*large black arrow,* middle row), which continues to increase for 11 hours (*large black arrow,* bottom row) and allows superior delineation of the tumor/brain border over nonenhanced baseline images.

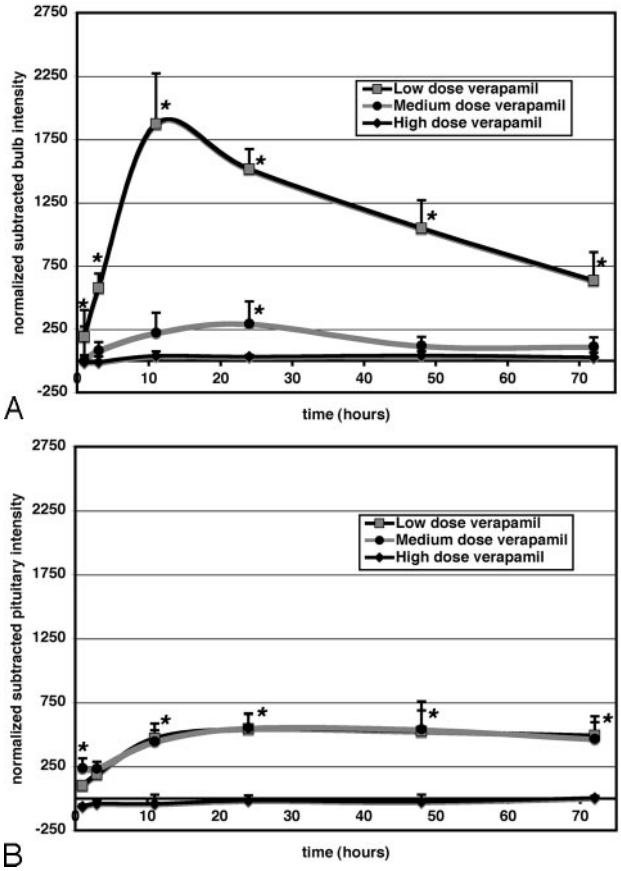

Fig 3. Verapamil alters Mn^{2+} uptake in the olfactory bulb and pituitary gland. Change in intensity with time in the olfactory bulb was modulated by different doses of verapamil injected intranasally before $MnCl_2$ administration (*A*). In the same subjects, VOI in the pituitary indicates that low- and medium-dose verapamil have a nearly identical effect on uptake; however, uptake remains virtually extinct with a high dose (*B*). The vertical axis represents normalized intensity for VOIs in the right olfactory bulb and in the pituitary gland that have been subtracted from baseline values. The horizontal axis is time in hours postinjection of $MnCl_2$. Error bars show the SD of mean change in intensity. The asterisk indicates differences that reached statistical significance ($P \leq .05$).

Manganese uptake versus tumor size and peak glucose metabolism*

	Rat 2	Rat 3	Rat 4
Average % change MR image	40.1	35.7	24.9
Peak FDG uptake	0.82	0.84	0.71
Tumor size (mm^2)	162	113	45

* Average percentage change on MR image was calculated as intensity 11 hours post-$MnCl_2$: baseline intensity/baseline intensity × 100 from a large VOI over the individual tumor. Peak FDG was calculated as the peak normalized glucose metabolic rate measured in the entire tumor. Tumor size in square millimeters was calculated from the MR image using pixel size and summed areas of 2D regions of interest hand drawn on each section.

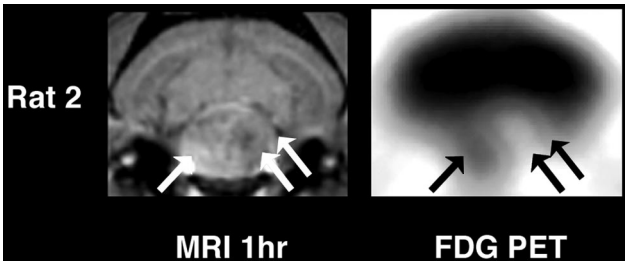

Fig 4. FDG-PET versus Mn-MR imaging: single subject. Coronal sections through pituitary tumor of rat 2. Left column shows tumor 1 hour after intranasal administration of the calcium analog Mn^{2+}. Right column shows an FDG-PET scan of tumor glucose metabolism. Single arrows (white on MR imaging, black on PET) indicate region of high glucose metabolism correlating with high calcium influx. Double arrows (white on MR imaging, black on PET) indicate low glucose metabolism and calcium influx in the area of necrosis.

Coronal and sagittal MR images obtained 11 hours following intranasal injection of Mn^{2+} demonstrated a large pituitary adenoma in each rat extending to the suprasellar cistern and the central skull base. Although the adenomas from all 3 rats appeared similar on MR images, we did note some distinct characteristics that may correspond to individual histopathologic features (Fig 5). Marked high signal intensity of the pituitary adenoma in rat 1 indicated an intense tumor uptake of Mn^{2+}. Most interesting, the tumor morphology from this rat was more solid, with moderate areas of atypia and fewer dilated vascular areas or hemorrhages compared with rats 2 and 3 (Fig 5, upper right panel, H&E). There was heterogeneous contrast enhancement in rats 2 and 3, and the degree of Mn^{2+} uptake was less intense compared with that in rat 1. This may be due to the relative increase in both vascular/cystic spaces as well as the presence of hemorrhage in these tumors. In support of this, a focal area of marked low signal intensity was noted in the superior right lateral aspect of the pituitary tumor in rat 3, corresponding to a focus of hemorrhage on pathology (Fig 5, number sign).

GH3 Cells Show Dose-Related Mn^{2+} Uptake In Vitro

In vivo cell culture of GH3 pituitary adenoma cells with increasing concentrations of $MnCl_2$ indicated a dose-response relationship of Mn^{2+} uptake as assessed by mass spectrophotometry. Mn^{2+} content of cultured cells incubated with 0.25-mM and 0.5-mM $MnCl_2$ (3.06 ± 1.22 and 10.71 ± 3.41 pg/cell, respectively) was significantly higher than the Mn^{2+} content of control samples that were incubated with vehicle alone (0.108 pg/cell, $P \leq .01$) (Fig 6).

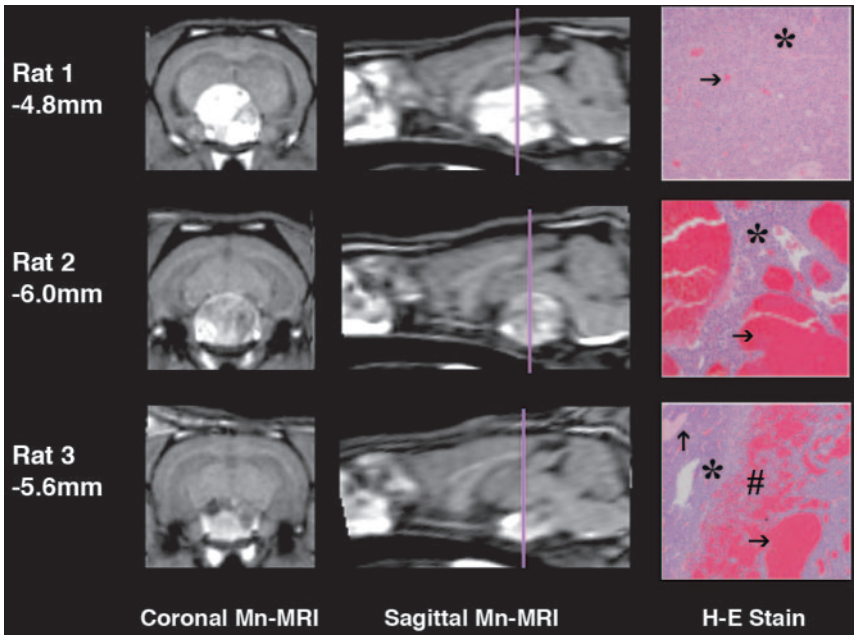

Fig 5. Mn-MR images of individual subjects show correspondence to H&E stain. Coronal 3D-SPGR images through a pituitary adenoma at 11 hours post-$MnCl_2$ injection show different patterns of uptake between different subjects. Histologic sections are from paraffin-embedded H&E-stained pituitary tumors. Rat 1: The tumor is composed of principally solid sheets of neoplastic cells (*asterisk*) and a few small-caliber capillaries (*arrow*) with minimal hemorrhage. Images for rat 1 indicate intense more uniform uptake of Mn^{2+}. Rat 2: Note the large dilated vascular and cystic spaces within the tumor section (*arrow*) and cords of neoplastic cells (*asterisk*). Rat 3: Note area of hemorrhage within the tumor parenchyma (*number sign*) and dilated vascular and cystic spaces (*arrows*) within cords of neoplastic cells (*asterisk*). MR images of rats 2 and 3 have less-intense uptake with a more heterogeneous appearance, which may correspond to hemorrhage and cystic spaces on pathology. Purple line indicates location of the coronal section on the sagittal image. All sagittal sections are from the midline. The number beneath each subject indicates the distance of the coronal section in millimeters from the bregma landmark.[20] (All histologic sections, original magnification ×10).

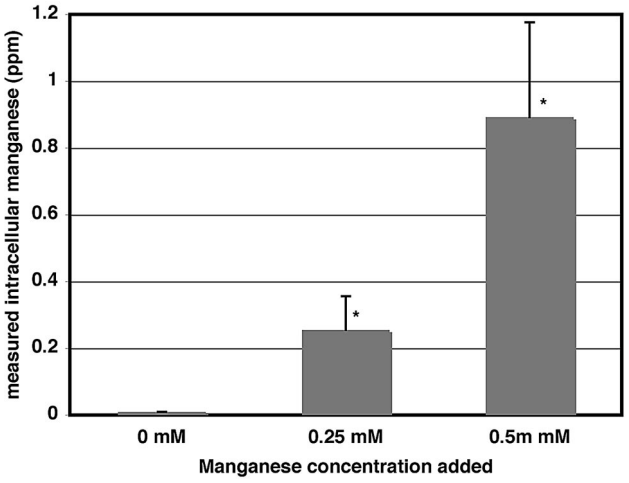

Fig 6. Manganese content in cells is increased with higher concentrations of $MnCl_2$. Graph shows intracellular Mn^{2+} (parts per million [ppm]) for 2 concentrations of $MnCl_2$ incubated with GH3 cells compared with vehicle alone. Error bars show SD of multiple samples. The asterisk indicates significant increase ($P \leq .01$).

Discussion

This study shows evidence that calcium influx is increased for pituitary adenomas. Because the mechanisms for neuroendocrine release through extracellular calcium influx are well-characterized,[13,14] it seems logical to evaluate pituitary function, particularly pathologic function, through the development of an in vivo calcium influx indicator. The physiologic properties of Mn^{2+} as a calcium analog have been investigated thoroughly by many institutions and in various experimental settings.[7-9] The ability to assess Mn^{2+} uptake dynamically in different tissues through MR imaging provides not only morphologic information that is distinguished by an intracellular agent but also functional information related to the neuroendocrine activity of the pituitary gland, both normal and abnormal (neoplastic) tissue. The results in this study show that calcium influx is more rapid as well as of greater magnitude in adenomas in comparison with normal pituitary glands in aged Sprague Dawley rats. Further investigations into this finding may be able to distinguish more directly normal tissue from adenoma before or even, with intraoperative MR imaging, during surgical resection of tumor tissue.

In addition, these results showed that verapamil, a calcium channel blocker, mitigated the Mn^{2+}-induced intensity change on MR images, and our in vitro results confirmed that the Mn^{2+} is directly taken up into GH3 cells. Thus, with the uptake of Mn^{2+} occurring as intracellular, the degree of the invasiveness of the tumor maybe more accurately delineated than with conventional extracellular MR contrast agents. In the use of these agents such as gadolinium, differences in the dynamic release of the contrast agent from the vasculature to the interstitial space was examined to differentiate normal pituitary gland from adenoma.[24-27] These studies found that factors such as surrounding microvasculature, arterial blood supply, size of adenoma, and tumor type (fibrous versus soft) affected the variability in clinical diagnoses.[26] Although we have yet to perform such rigorous investigation on this newly proposed imaging method, the fact that Mn^{2+} enters into cells by a means that is directly related to the activity of a cell suggests the potential for improved clinical pituitary tumor assessment. Rapid absorption from the nasal cavity into the blood was indicated by the intensity change seen in the carotid artery at 1 hour postinjection.

Although the study size was limited to only a few adenoma cases, the average peak calcium influx showed good correlation to both the peak metabolism and the size of the tumor. The use of FDG-PET in the diagnosis of pituitary adenoma has been reported in case reports and limited investigations, particularly with Cushing disease, and as an imaging tool before radiosurgery resection.[28-31] One difficulty that limits the utility of FDG-PET for pituitary adenoma imaging is that brain uptake is usually higher than that of the tumor, so images must be carefully registered to MR images to delineate accurately the boundary between tumor and brain.[32] Even so, as was found in our study, active tumor areas in these investigations show increased metabolism as opposed to areas of necrosis,

hemorrhage, or normal pituitary tissue. In addition, the alternative use of calcium influx as an indicator of pituitary hyperactivity gives more neuroendocrine tissue–specific information than merely assessing overall metabolism. The correlation that we found of calcium influx to tumor size may suggest that these tumors were hormone-secreting. However, this conclusion is merely speculative because serum hormone levels were not measured in this study. In human pituitary adenomas, large tumors tend to be nonsecreting and small ones tend to be hormone-secreting.[17] The simple reason is that secreting tumors tend to manifest clinical symptoms sooner, so they are uncovered when they are still small. The next step of this investigation will need to assess serum hormone levels as they correlate to calcium influx. It would be interesting to see if nonsecreting adenomas have increased calcium influx. However, even in the case of nonsecreting adenomas, Mn-MR imaging may still be used to delineate accurately the extent of the invasiveness of the tumor.

All of our subjects had adenomas of the pars distalis by histopathologic diagnosis, which is consistent with the literature because most spontaneous pituitary adenomas in Sprague Dawley rats are prolactin-producing adenomas, with the reported incidence ranging from 47%–64%.[33,34] Prolactin-secreting adenomas are also common in Fisher rats; however, tumors may be composed of prolactin and growth hormone–producing cells.[35] In our subjects that had spontaneous adenoma, immunohistochemical diagnosis of tumor type was not performed, and the effect, if any, on calcium influx in pituitary adenomas with differences in hormone-producing cells remains to be determined.

A potential drawback in the development of Mn^{2+} as a clinical imaging agent is the issue of toxicity. Overexposure to Mn^{2+} has been shown to have toxic side effects, particularly in the brain, with parkinsonian-type symptoms a feature of manganism.[36-38] However, some amount of Mn^{2+} is required by the body for cellular processes and as protein components.[39] There is an acceptable dose range in which a single administration would not be toxic but would still permit measurable contrast enhancement to the pituitary gland.[40] There are currently several US Food and Drug Administration–approved Mn^{2+}-based MR imaging contrast agents that are used for imaging. In one study, intravenously administered mangafodipir trisodium was imaged, and increased enhancement was seen in the pituitary and choroid plexus as well as in organs such as the liver, pancreas, and kidney.[41]

It is interesting to speculate if this technique could be developed for safe use in human subjects and how it might be applied to address a valid clinical question. All of the subject animals in this study had macroadenomas, but the diagnosis of macroadenomas in human patients does not pose a problem. However, detection of microadenomas can be difficult. This raises the question of whether microadenomas behave metabolically similar to macroadenomas, and for similar hormonally active tumors, there is every reason to believe they do. If that proves to be true, then the only limitation to the size of the tumor that can be detected is dependent on the avidity of a given lesion for Mn^{2+} and the contrast difference-to-noise level that can be achieved. Such a technique could be useful for detection of small microadenomas or for distinguishing a microadenoma from a pituitary "incidentaloma," which is not reliably possible today. In particular, such a technique might prove particularly useful in detection and localization of adrenocorticotropic hormone–secreting tumors in patients with Cushing Disease because these are notoriously difficult and often impossible to detect by imaging studies.

Conclusion

In conclusion, as was proposed by our hypothesis, the results indicate that pituitary adenomas have increased activity-dependent calcium influx compared with normal pituitary glands in aged rats. This physiologic property suggests the potential for Mn-MR imaging in the clinical work-up of human pituitary and other neuroendocrine tumors. Further studies with larger subject cohorts and more detailed pathologic confirmation will be needed to better characterize the utility of this imaging technique in the clinical setting.

Acknowledgments

The authors thank Jeff Stevenson for his useful comments regarding MR imaging and Barbara Lewellen for technical assistance with the PET scanning.

References

1. Leergaard TB, Bjaali JB, Devor A, et al. **In vivo tracing of major rat brain pathways using manganese-enhanced magnetic resonance imaging and three-dimensional digital atlasing.** *Neuroimage* 2003;20:1591–600
2. Pautler RG, Silva AC, Koretsky AP. **In vivo neuronal tract tracing using manganese-enhanced magnetic resonance imaging.** *Magn Reson Med* 1998;40:740–48
3. Saleem KS, Pauls JM, Augath M, et al. **Magnetic resonance imaging of neuronal connections in the macaque monkey.** *Neuron* 2002;34:685–700
4. Van der Linden A, Verhoye M, Van Meir V, et al. **In vivo manganese-enhanced magnetic resonance imaging reveals connections and functional properties of the songbird vocal control system.** *Neuroscience* 2002;112:467–74
5. Watanabe T, Michaelis T, Frahm J. **Mapping of retinal projections in the living rat using high-resolution 3D gradient-echo MRI with Mn2+-induced contrast.** *Magn Reson Med* 2001;46:424–29
6. Cross DJ, Minoshima S, Anzai Y, et al. **Statistical mapping of functional olfactory connections of the rat brain in vivo.** *Neuroimage* 2004;23:1326–35
7. Narita K, Kawasaki F, Kita H. **Mn and Mg influxes through Ca channels of motor nerve terminals are prevented by verapamil in frogs.** *Brain Res* 1990;510:289–95
8. Pautler RG, Koretsky AP. **Tracing odor-induced activation in the olfactory bulbs of mice using manganese-enhanced magnetic resonance imaging.** *Neuroimage* 2002;16:441–48
9. Takeda A, Kodama Y, Ishiwatari S, et al. **Manganese transport in the neural circuit of rat CNS.** *Brain Res Bull* 1998;45:149–52
10. Aoki I, Tanaka C, Takegami T, et al. **Dynamic activity-induced manganese-dependent contrast magnetic resonance imaging (DAIM MRI).** *Magn Reson Med* 2002;48:927–33
11. Lin YJ, Koretsky AP. **Manganese ion enhances T1-weighted MRI during brain activation: an approach to direct imaging of brain function.** *Magn Reson Med* 1997;38:378–88
12. Lee JH, Koretsky AP. **Manganese-enhanced magnetic resonance imaging.** *Curr Pharm Biotechnol* 2004;5:529–37
13. Ozawa S, Sand O. **Electrophysiology of excitable endocrine cells.** *Physiol Rev* 1986;66:887–952
14. Zimber MP, Simasko SM. **Recruitment of calcium from intracellular stores does not occur during the expression of large spontaneous calcium oscillations in GH(3) cells and lactotropic cells in primary culture.** *Neuroendocrinology* 2000;72:242–51
15. Kimata-Hayashi N, Takano K, Yasufuku-Takano J, et al. **Mechanism of adrenomedullin-induced prolactin release from human prolactin-releasing adenoma cells.** *Endocr J* 2005;52:769–73
16. Mondok A, Szeifert GY, Mayer A, et al. **Treatment of pituitary tumors: radiation.** *Endocrine* 2005;28:77–85
17. Bonneville JF, Bonneville F, Cattin F. **Magnetic resonance imaging of pituitary adenomas.** *Eur Radiol* 2005;15:543–48
18. Maes F, Collignon A, Vandermeulen D, et al. **Multimodality image registration by maximization of mutual information.** *IEEE Trans Med Imaging* 1997;16:187–98

19. Press WH, Flannery BP, Teukolsky SA, et al. *Numerical Recipes in C.* Cambridge, UK: Cambridge University Press; 1988
20. Paxinos G, Watson C. *The Rat Brain in Stereotaxic Coordinates*. 4th ed. San Diego, Calif: Academic Press; 1998
21. Venot A, Lebruchec JE, Golmard JL, et al. **An automated method for the normalization of scintigraphic images** *J Nucl Med* 1983;24:529–31
22. Minoshima S, Koeppe RA, Fessler JA, et al. **Integrated and automated data analysis method for neuronal activation studies using [O-15]water PET.** In: Uemura K, Lassen NA, Jones T, Kanno I, eds. *Quantification of Brain Function, Tracer Kinetics and Image Analysis in brain PET*. Amsterdam, the Netherlands; Excerpta Medica; 1933:409–415
23. Carlton WW, Gries CL. **Adenoma and carcinoma, pars distalis, rat**. In: Jones TC, ed. *Endocrine System (Monographs on Pathology of Laboratory Animals)*. New York: Springer-Verlag; 1986:134–45
24. Doppman JL, Frank JA, Dwyer AJ, et al. **Gadolinium DTPA- enhanced MR imaging of ACTH-secreting microadenomas of the pituitary gland.** *J Comput Assist Tomogr* 1988;12:728–35
25. Finelli DA, Kaufman B. **Varied microcirculation of pituitary adenomas at rapid, dynamic, contrast-enhanced MR imaging.** *Radiology,* 1993;189:205–10
26. Kanou Y, Arita K, Kurisu K, et al. **Clinical implications of dynamic MRI for pituitary adenomas: clinical and histologic analysis.** *J Clin Neurosci* 2002;9:659–63
27. Tabarin A, Laurent F, Catargi B, et al. **Comparative evaluation of conventional and dynamic magnetic resonance imaging of the pituitary gland for the diagnosis of Cushing's disease.** *Clin Endocrinol (Oxf)* 1998;49:293–300
28. Bergstrom M, Muhr C, Lundberg PO, et al. **PET as a tool in the clinical evaluation of pituitary adenomas.** *J Nucl Med* 1991;32:610–15
29. Campeau RJ, David O, Dowling AM. **Pituitary adenoma detected on FDG positron emission tomography in a patient with mucosa-associated lymphoid tissue lymphoma.** *Clin Nucl Med* 2003;28:296–98
30. De Souza B, Brunetti A, Fulham MJ, et al. **Pituitary microadenomas: a PET study.** *Radiology* 1990;177:39–44
31. Komori T, Martin WH, Graber AL, et al. **Serendipitous detection of Cushing's disease by FDG positron emission tomography and a review of the literature.** *Clin Nucl Med* 2002;27:176–78
32. Muhr C. **Positron emission tomography in acromegaly and other pituitary adenoma patients.** *Neuroendocrinology* 2006;83:205–10
33. McComb D, Kovacs JK, Beri J, et al. **Pituitary adenomas in old Sprague-Dawley rats: a histologic, ultrastructural, and immunocytochemical study.** *J Natl Cancer Inst* 1984;73:1143–66
34. Sandusky GE, Van Pelt CS, Todd GC, et al. **An immunocytochemical study of pituitary adenomas and focal hyperplasia in old Sprague-Dawley and Fischer 344 rats.** *Toxicol Pathol* 1988;16:376–80
35. MacKenzie WF, Boorman GA. **Pituitary gland.** In: Boorman GA, ed. *Pathology of the Fischer Rat.* San Diego, Calif: Academic Press; 1990:424–25
36. Crossgrove J, Zheng W. **Manganese toxicity upon overexposure.** *NMR Biomed* 2004;17:544–53
37. Martin CJ. **Manganese neurotoxicity: connecting the dots along the continuum of dysfunction.** *Neurotoxicology* 2006;27:347–49
38. Verity M.A. **Manganese neurotoxicity: a mechanistic hypothesis.** *Neurotoxicology* 1999;20:489–97
39. Aschner M, Vrana KE, Zheng W. **Manganese uptake and distribution in the central nervous system (CNS)**. *Neurotoxicology* 1999;20:173–80
40. Gianutsos G, Morrow GR, Morris JB. **Accumulation of manganese in rat brain following intranasal administration.** *Fundam Appl Toxicol* 1997;37:102–05
41. Wang C, Gordon PB, Hustvedt SO, et al. **MR imaging properties and pharmacokinetics of MnDPDP in healthy volunteers**. *Acta Radiol* 1997;38(4 Pt 2): 665–76